Fischer–Tropsch synthesis in polyethylene glycol with amorphous iron nanocatalysts prepared by chemical reduction in various solvents

Xiaofan Cheng [a,b,c], Baoshan Wu [a,b,*], Yong Yang [a,b], Hongwei Xiang [a,b], Yongwang Li [a,b]

[a] State Key Laboratory of Coal Conversion, Institute of Coal Chemistry, Chinese Academy of Sciences, Taiyuan, Shanxi 030001, PR China
[b] National Engineering Laboratory for Indirect Coal Liquefaction, Institute of Coal Chemistry, Chinese Academy of Scienes, Taiyuan, Shaixi 030001, PR China
[c] Graduate University of Chinese Academy of Sciences, Beijing 100049, PR China

ARTICLE INFO

ABSTRACT

Amorphous iron nanocatalysts were prepared by chemical reduction using various solvents and dispersed in polyethylene glycol (PEG) for Fischer–Tropsch synthesis (FTS). The results indicated that the as-prepared catalysts were mainly amorphous Fe-B or Fe-B/α-Fe nanoalloys with a surface layer of oxides of iron and boron. The preparation solvents had a significant influence on the morphology, phase composition and surface property of these catalysts. Under reaction conditions of 3.0 MPa syngas ($H_2/CO = 2$) and 200 °C, the catalyst prepared in water exhibited the highest FTS activity (0.83 mol_{CO} mol_{Fe}^{-1} h^{-1}). This high activity is attributed to its high iron content and extent of reduction on the surface as well as high iron carbides formed during reaction. The products or catalysts can be easily separated after reaction.

© 2010 Elsevier B.V. All rights reserved.

1. Introduction

Fischer–Tropsch synthesis (FTS) is the main process for catalytic conversion of syngas derived from coal, natural gas and biomass to liquid fuels and other chemicals. Over the past few decades, conventional catalysts for FTS have been widely investigated and have gained significant advancements in practical and potential applications [1,2]. Due to the limitations of bulk materials, it seems impossible to design, adjust, and control the properties of traditional catalysts effectively at a molecular level. Consequently, exploring novel catalysts or catalytic systems with excellent catalytic performances is becoming one of the most exciting challenges in FTS.

Amorphous nanocatalysts have attracted growing attention in catalysis due to their interesting intrinsic properties, e.g. high surface area, short-range order and long-range disorder. Moreover, the presence of highly surface coordinated unsaturated sites facilitates adsorption and surface reactions. They have exhibited excellent catalytic performances in some organic reactions because of their unique characteristics quite different from those of bulk materials and crystalline alloys [3–5]. One of the challenging problems for nanocatalysts is the congregation of metallic nanoparticles during the reaction due to high surface energy. This tendency to agglomer-

ate limits their utility as industrial catalysts. To solve this problem, stabilizers including oxides [6], charcoal [7], and nanotubes [8] have been used as supports for metallic nanoparticles. In recent years, some innovative stabilizers and media [9] such as dendrimers [10], polymers [11], specific ligands [12], surfactants [13] and ionic liquids [14] have appeared and attracted increasing attention because of their unique properties.

Soluble nanoparticle catalysts usually indicate nanoparticles that are well dispersed in solutions by means of soluble stabilizers. The soluble nanoparticles with controllable sizes and morphologies are freely rotational and three-dimensional in reaction systems. They have been widely used in various organic reactions due to their potentially higher catalytic efficiency under milder operation conditions than traditional supported catalysts [14,15]. So far, studies and reports on soluble nanocatalysts used in FTS are scarce except for aqueous-soluble Ru nanoclusters [16] and Co nanoparticles in ionic liquids [17].

Iron, as a cheap, active and selective FTS catalyst, is seldom used in solvent systems. The major reason is that pure iron is easily oxidized or carburized and the active phases may be quite different from other transition metal catalysts. It is worth more attention and interest that an amorphous iron nanocatalyst is well dispersed in a chosen liquid system and may exhibit high FTS activity. This catalytic system requires amorphous iron nanoparticles, suitable solvent and soluble stabilizing additive. Polyethylene glycol (PEG) is a cheap, readily available, safe and stable polymer. It has been used previously as a stabilizer for the preparation of nanoparticles in var-

* Corresponding author. Tel.: +86 0351 7117141.
E-mail address: wbs@sxicc.ac.cn (B. Wu).

ious solvents [18]. Recently, liquid short-chain PEG has emerged as a new green solvent due to its high polarity and excellent thermal stability in catalytic reactions particularly in the hydrogenation of various organic substrates [19,20]. In most cases, transition metal catalysts can be dissolved in PEG and appear to be stable without the use of specially designed stabilizers. In addition, using PEG as a solvent can simplify catalyst/product separation due to its low miscibility with most organic compounds. Therefore, amorphous iron nanoparticles in PEG phase should be one of ideal choices for the improvement of traditional FTS catalytic systems.

In the present work, a series of amorphous iron nanocatalysts for FTS were prepared by chemical reduction in various solvents (ethylene glycol, ethylene glycol/water and water). These nanocatalysts were dispersed in PEG with a molecular weight of 400 as reaction solvent and then tested for FTS performance. Various characterization techniques were used to determine the influence of preparation solvents on the morphology, phase composition, surface property and FTS performance of the amorphous iron catalysts and the results are discussed in detail. The correlation of the catalytic activities to the structural properties was tentatively established.

2. Experimental

2.1. Catalyst preparation

The iron nanocatalysts were synthesized by the chemical reduction method [21]. KBH_4 was used as the reducing agent. Mixtures of ethylene glycol and water in volumetric ratios of 2:1 and 1:2 as well as the pure components were used to dissolve the iron salt. Typically, an aqueous solution of 2.4 M KBH_4 (10 ml) was added dropwise to 0.2 M $FeCl_3 \cdot 6H_2O$ solution (30 ml) with vigorous stirring under an inert atmosphere of nitrogen. The solution turned black immediately with evolution of hydrogen gas. After the gas evolution subsided, stirring continued for 30 more minutes to allow the reaction to complete. A permanent magnet was used to remove the black precipitate from the solution. The precipitate was then washed with absolute ethanol three times, followed by washing in PEG two times, and finally stored in 40 g PEG for catalytic tests.

The as-prepared catalysts were designated Fe-*x*, with *x* representing the preparation solvents. These catalysts were denoted Fe-E, Fe-E2W1, Fe-E1W2 and Fe-W where E and W refer to ethylene glycol and water and the numbers represent the volumetric ratios of solvents.

2.2. Catalyst characterization

The particle size and morphology were determined by JEOL JEM-1011 transmission electron microscopy (TEM). The nanoparticles were dispersed in dilute ethanol by ultrasonication for 30 min, and then one drop of solution was placed on the surface of a carbon coated copper grid. The size distributions of the nanoparticles were estimated from ensembles of 150 particles found in arbitrary chosen areas of the enlarged micrographs.

X-ray diffraction (XRD) patterns of the catalysts samples were obtained on a D/max-2500 X-ray diffraction meter (Rigaku, Japan) equipped with a Cu Kα source (λ = 0.154 nm) and a Ni filter operated at 40 kV, 100 mA. The range of collection was 10–80° at a scanning rate of 4 ($°$) min^{-1} and a step length of 0.01°. The sample for XRD analysis was washed three times by absolute ethanol, and finally placed into liquid paraffin.

The composition of the samples was determined by elemental analyses using inductively coupled plasma atomic emission spectroscopy (ICP-AES) (Atom scan 16).

Differential scanning calorimetry (DSC) measurements were conducted under N_2 atmosphere on a METTLER TOLEDO DSC.

The samples were scanned over the range 50–800 °C at a rate of 10 °C/min to investigate the crystallization processes of the amorphous structure.

The Mössbauer spectra (MES) (Austin, USA) were obtained on a time-mode spectrometer (S-600), with a CANBERRA Series 40 MCA constant-acceleration drive and a triangular reference signal at room temperature, using a 25-mCi ^{57}Co in Pd matrix. Magnetic hyperfine fields were calibrated with 15 μm α-Fe. The data were obtained by computer and the spectra were operated by least squares fitting routine. Hyperfine parameters, isomer shift (IS), quadruple splitting (QS), and magnetic hyperfine field (H_{hf}) were used to identify the spectral components. Iron-phase compositions were determined by integrating the areas of the adsorption peaks.

X-ray photoelectron spectra (XPS) were recorded with a Thermo VG Scientific Sigma Probe spectrometer. The XPS patterns were collected using Al Kα radiation at a voltage and current of 20 kV and 30 mA, respectively. The binding energy values were calibrated using C 1s = 284.6 eV as a reference.

2.3. Catalytic testing

In a typical experiment, the freshly prepared iron nanoparticles were dispersed in 40 g PEG and placed in a 100-ml stainless steel autoclave. Then the reactor was purged three times with syngas and sealed at a syngas pressure of 3.0 MPa. All syngas (H_2/CO = 2) fed to the reactor first passed through a series of purification traps to remove iron carbonyls, water and other impurities. The autoclave was kept at 200 °C with stirring at 800 rpm for about 12 h. After the reaction, the autoclave was cooled to room temperature. Catalytic activity was monitored by the pressure drop.

The gas mixture was analyzed by an Agilent 6890N (HP) gas chromatograph (GC) with a 5A molecular sieve column (Ar carrier) and an Al_2O_3 column (N_2 carrier) equipped with a TCD and an FID. Gas components were determined by the methane concentration correlation method. CO_2 was measured using an Agilent 4890D GC (HP) equipped with a TCD (H_2 carrier) and quantified by the external standard method. The oil was extracted in cyclohexane and analyzed by an Agilent 6890N (HP) GC with UA + -(HT) stainless steel capillary column (FID, N_2 carrier) using decahydronaphthalene as the internal standard.

The activity was expressed as mol of CO (or H_2) converted per mol Fe per hour. The CO_2 selectivity (mol%) denoted the molar ratio of the produced CO_2 to the total converted CO. The hydrocarbon distribution (wt%) for C_n represented the mass ratio of C_n to the total hydrocarbons which could be collected.

3. Results and discussion

3.1. Morphology and size

TEM images of the iron nanocatalysts prepared in various solvents are shown in Fig. 1a–d. The size distributions of these nanoparticles are listed in Table 1. The four nanocatalysts displayed irregular spherical or chainlike morphologies with blurry boundaries due to particle agglomeration. Since the reduction of metallic ions by BH_4^- was strongly exothermic, it was difficult to control the reduction process resulting in broadly dispersed particle sizes. The nanoparticles synthesized in ethylene glycol had the smallest particle size of 3–8 nm, and the particle size increased from 20–45 to 30–60 nm with an increase in water content of the preparation system.

Fig. 2a–d shows the TEM morphologies of the iron nanocatalysts after FTS reaction. Table 1 lists their corresponding particle sizes. Comparing Fig. 1 and Fig. 2 reveals changes in morphologies of the respective catalysts as a result of the reaction. The cata-
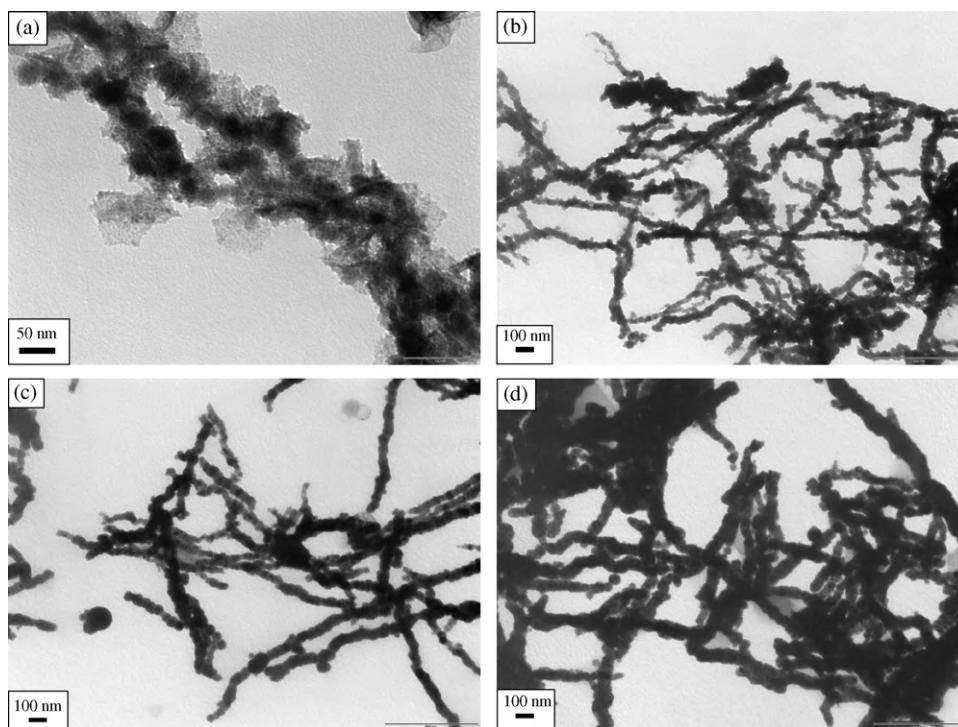
Fig. 1. (a–d) TEM morphologies of the iron nanocatalysts prepared in various solvents: (a) E, (b) E2W1, (c) E1W2, and (d) W.

lyst prepared in ethylene glycol clearly agglomerated from 3–8 to 30–70 nm, whereas the particle sizes for the Fe-E2W1 redistributed and broadened slightly from 20–45 to 20–50 nm. The particle sizes for the Fe-E1W2 were unchanged, and the particle sizes for the catalyst prepared in water became smaller to some extent after reaction. Two possible reasons for changes in particle sizes can be given. First, the catalysts underwent obvious phase changes

and re-crystallization during FTS reaction. Second, the reaction medium may impose different effects on nanoparticles with different sizes. During FTS reaction, PEG molecules could adsorb on the surface of the nanoparticles and help to restrain the coagulation of nanoparticles by means of their excellent steric stabilization effects [9]. Catalysts prepared in ethylene glycol/water mixture and water avoided expected agglomeration, whereas the Fe-E catalyst
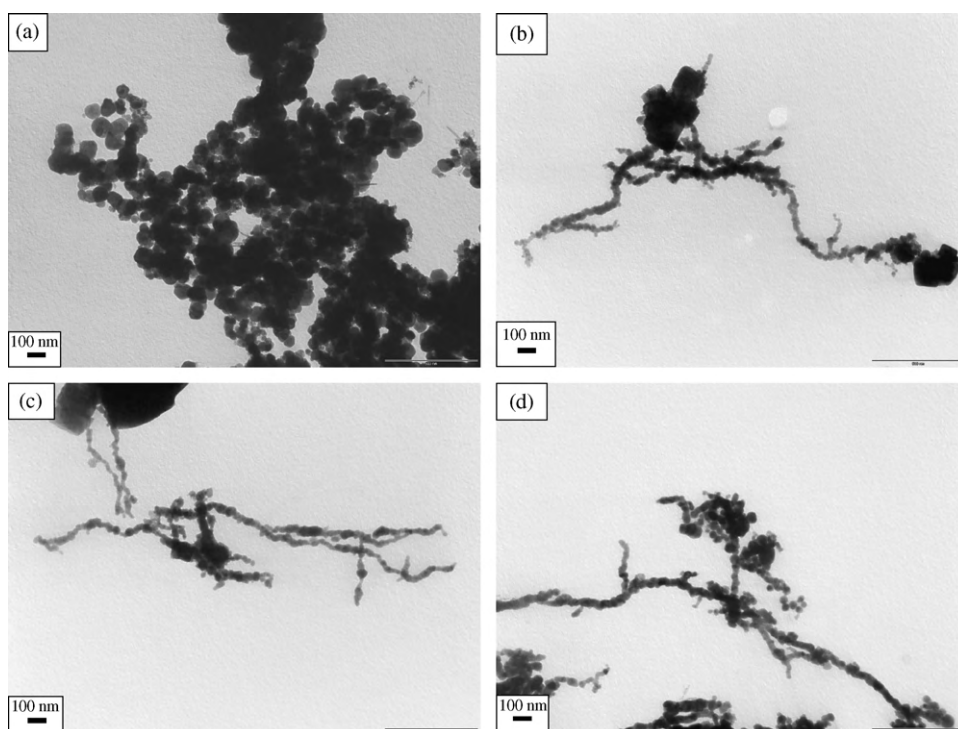

Fig. 2. (a–d) TEM micrographs of the iron nanocatalysts after reaction. The preparation solvents are (a) E, (b) E2W1, (c) E1W2, and (d) W, respectively.

Table 1
Textural properties of the iron nanocatalysts.

Catalyst	Particle size (nm)		Composition[a] (at%)	
	Reduced	Reacted	Bulk[b]	Surface[c]
Fe-E	3–8	30–70	$Fe_{79.19}B_{20.81}$	$Fe_{81.07}B_{18.93}$
Fe-E2W1	20–45	20–50	$Fe_{82.11}B_{17.89}$	$Fe_{82.56}B_{17.44}$
Fe-E1W2	20–50	20–50	$Fe_{84.06}B_{15.94}$	$Fe_{84.96}B_{15.04}$
Fe-W	30–60	20–55	$Fe_{86.25}B_{13.75}$	$Fe_{87.85}B_{12.15}$

at%: atomic ratio.
[a] The composition of reduced catalysts.
[b] Determined by ICP-AES.
[c] Calculation based on XPS peak areas.

with the smallest particles induced significant agglomeration due to extremely high surface energy.

3.2. Bulk phase characteristic

Fig. 3 illustrates the XRD patterns of the as-prepared catalysts in various solvents. A single broad peak around $2\theta = 45°$ indicates the amorphous nature of the samples [21]. This structure is further confirmed to be the amorphous iron-metalloid alloy by the DSC curves and Mössbauer spectra given below. It is clear that the single diffraction peak became sharper gradually suggesting that the particle size increased correspondingly, which agrees with the aforementioned TEM result.

The bulk composition of the prepared catalysts was determined by ICP-AES (listed in Table 1). In ethylene glycol, a relatively B-enriched alloy was formed. The B content in Fe-B alloys decreased gradually with increasing water added to ethylene glycol. The B content of the catalyst prepared in water was lowest. Decrease in the B content may be due to the relative easiness of BH_4^- hydrolysis in the preparation mediums with higher water concentrations, which would reduce the acidity of the reaction solution and form amorphous alloys with lower B content [22].

DSC was carried out to characterize the crystallization process of the amorphous iron nanoparticles prepared in various solvents. As shown in Fig. 4, the crystallization of the Fe-E sample involved two steps: the structural rearrangement and the crystallization of the amorphous Fe-B alloy with two exothermic peaks at around 274 and 520 °C [5]. Other samples displayed only one exothermic peak in the range between 326 and 460 °C. These exothermic processes are believed to be associated with the crystallization of the amorphous Fe-B phases. The exothermic peak became weaker and shifted to lower temperature with the increase of water added to the solvents. That is, the lower boron concentration leads to the
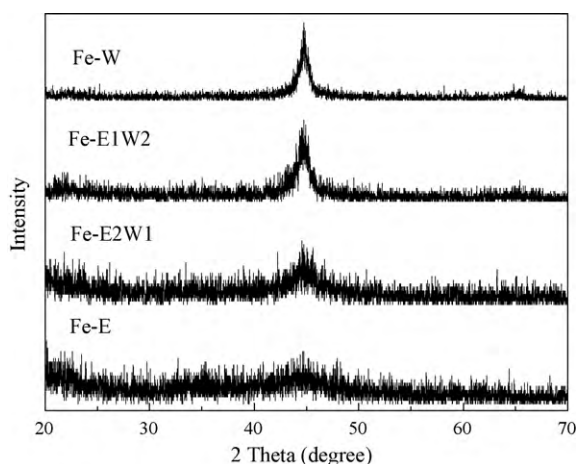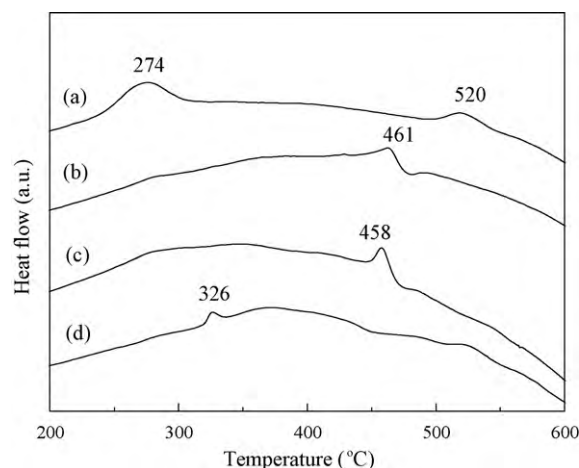

Fig. 4. DSC curves of the (a) Fe-E, (b) Fe-E2W1, (c) Fe-E1W2, and (d) Fe-W catalyst samples.

lower crystallization temperature. The stability of the amorphous phase decreased with a decrease in boron content.

The iron-phase composition was quantitatively determined using Mössbauer spectroscopy. Fig. 5 shows the room temperature Mössbauer spectra of the iron nanocatalysts prepared in various solvents, and the corresponding Mössbauer parameters are listed in Table 2. As shown in Fig. 5, the Mössbauer spectra of these catalysts can be fitted with two ferromagnetic sextets and a superparamagnetic doublet. The broad sextets are characteristic of amorphous phases which can be identified as amorphous Fe-B alloys. In the case of the amorphous magnetic compounds, the Mössbauer spectra are rather complex because of broadening and/or overlapping of the resonance lines. Some authors have tried to describe the local environments in disordered structural alloys (through the values and the distribution of the hyperfine parameters observed by Mössbauer spectrometry). They assumed that the local environments in crystalline phase were similar to that of amorphous analogous systems [23]. Since there has been a lack of detailed information on Mössbauer parameters for amorphous Fe-B alloys in literature,
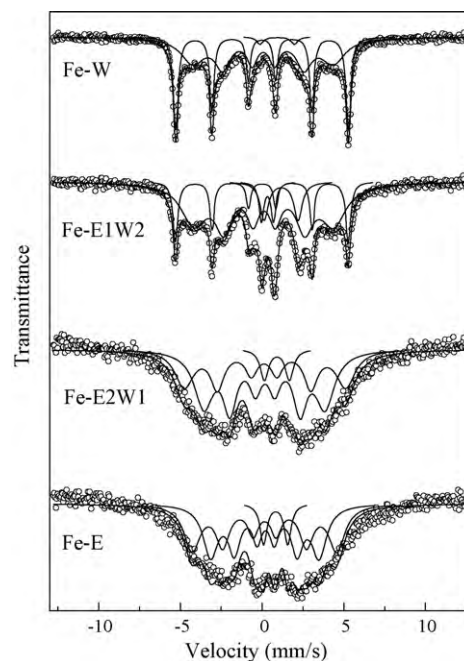

Fig. 3. XRD patterns of the iron nanocatalysts prepared in various solvents.

Fig. 5. Mössbauer spectra of the iron nanocatalysts prepared in various solvents.

Table 2
Mössbauer parameters of the iron nanocatalysts prepared in various solvents.

Catalyst	Phase	Mössbauer parameters			
		IS (mm/s)	QS (mm/s)	H_{hf} (kOe)	Area (%)
Fe-E	$Fe_{80}B_{20}$	0.15	−0.01	276	45.7
	$Fe_{62}B_{38}$	0.19	−0.05	207	46.4
	Fe^{2+}	0.83	1.48		7.9
Fe-E2W1	Fe_3B	0.15	0.05	307	37.5
	Fe_2B	0.16	−0.04	231	56.2
	Fe^{2+}	0.91	1.53		6.3
Fe-E1W2	α-Fe	0.00	−0.02	329	19.0
	$Fe_{80}B_{20}$	0.12	−0.02	266	65.7
	$Fe^{2+}BO_x$	1.17	2.08		9.6
Fe-W	α-Fe	0.00	0.01	329	42.1
	$Fe_{80}B_{20}$	0.07	−0.02	268	55.7
	$Fe^{2+}BO_x$	0.93	2.10		2.2

IS: the isomer shift; QS: the quadruple splitting; H_{hf}: the magnetic hyperfine field.

some parameters from crystalline Fe-B metallic phases were used in this study. Accordingly, the broad sextets with H_{hf} of about 300, 270, 230 and 200 kOe can be attributed to amorphous Fe_3B, $Fe_{80}B_{20}$, Fe_2B and $Fe_{62}B_{38}$, respectively [24,25]. The other sextet with an H_{hf} of 330 kOe is assigned to α-Fe. The doublets are ascribed to undetermined Fe^{2+}. The doublet with an IS of 1.0 mm/s and a QS of 2.0 mm/s has parameters typical of the ferrous cations in the $FeBO_x$ phase, represented as $Fe^{2+}BO_x$ [26]. These ferrous cations are probably coordinatively unsaturated due to large quadruple splitting and isomer shift [27]. As shown in Table 2, there are obvious differences in catalysts prepared in various solutions. Preparations in ethylene glycol and ethylene glycol/water (V/V, 2/1) mainly formed amorphous Fe-B alloys. With increasing water added to ethylene glycol, the value of IS decreased while that of QS increased until IS and QS values were close to those of standard α-Fe. This suggests that the B content in the amorphous Fe-B alloys decreased gradually, which agrees with the foregoing ICP-AES results, and that some of $Fe_{1−x}B_x$ was converted to α-Fe. These findings demonstrate that the solvent medium is important in determining the primary products after KBH_4 reduction, which is consistent with the conclusions of Glavee et al. [22].

The Mössbauer spectra of iron nanocatalysts after FTS reaction are shown in Fig. 6. Table 3 lists the iron-phase composition obtained by fitting the Mössbauer spectra. The sextets with H_{hf} around 487 and 456 kOe can be attributed to the tetrahedral site (A site) and octahedral site (B site) of Fe_3O_4, respectively. Other sextets are ascribed to χ-Fe_5C_2 and ε-$Fe_{2.2}C$ [28,29], and the doublets are superparamagnetic $Fe^{2+}BO_x$ [26]. As shown in Table 3, catalysts after reaction were mainly composed of Fe_3O_4. With increasing water added to the preparation system, the iron carbide content increased. The Fe-W catalyst after reaction had the highest iron carbides (20.4%). As shown above, the as-prepared iron nanocatalysts were mainly composed of amorphous Fe-B or Fe-B/α-Fe. It was previously reported that oxidation of $Fe_{1−x}B_x$ after exposure to air leads to conversion of Fe-B to α-Fe, then to an undetermined Fe^{2+} phase and finally to Fe_3O_4 [26]. Similarly, $Fe_{1−x}B_x$ converted to α-Fe first, followed by carbonization or oxidation quickly under FTS reaction conditions. There were continuous inter-conversions (repeated oxidation, reduction or carbonization) between iron carbides and iron oxides with magnetite eventually becoming the dominant phase.

3.3. Surface property

The XPS spectra of iron nanocatalysts are shown in Fig. 7. As shown in the pattern of Fe 2p, the profile of the Fe-E catalyst exhibits a broad peak with a binding energy around 710.0 eV for the Fe $2p_{3/2}$.
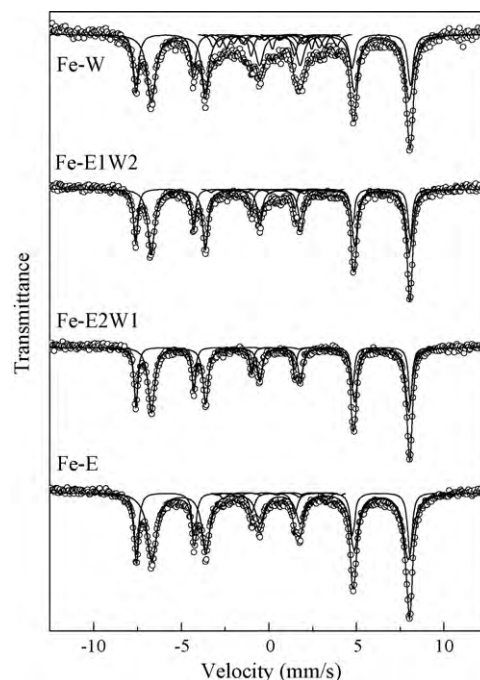

Fig. 6. Mössbauer spectra of the iron catalysts after reaction.

This peak can be attributed to contributions of a mixture of oxidized iron species (Fe^{2+} and Fe^{3+}) on the surface. The Fe $2p_{3/2}$ peak shifted to lower binding energy gradually with increasing water added to the preparation solvent suggesting that the extent of reduction of surface iron also enhanced correspondingly. For the Fe-W catalyst, a shoulder peak with a binding energy of 706.7 eV appeared. This shoulder peak is assigned to metallic iron in the sample. The relative areas of the two peaks for the Fe $2p_{3/2}$ indicate that iron remained mainly in the oxidized state on the surface of the sample. In comparison with pure iron (707 eV), the binding energy of the elemental iron shifted about −0.3 eV indicating that the metallic iron is alloyed with B. In alloys, partial electrons may be transferred from B to Fe. No appreciable intensity for elemental boron was observed at around 187 eV. Only an oxidized

Table 3
Mössbauer parameters of the iron nanocatalysts after reaction.

| Catalyst	Phase	Mössbauer parameters			
		IS (mm/s)	QS (mm/s)	H_{hf} (kOe)	Area (%)
Fe-E	$Fe_3O_4(A)$	0.25	−0.01	486	28.7
	$Fe_3O_4(B)$	0.64	0.00	456	66.1
	χ-Fe_5C_2	0.20	0.76	220	1.6
		0.20	0.41	186	3.6
Fe-E2W1	$Fe_3O_4(A)$	0.25	0.00	487	32.9
	$Fe_3O_4(B)$	0.65	0.00	457	64.8
	χ-Fe_5C_2	0.20	0.47	186	2.3
Fe-E1W2	$Fe_3O_4(A)$	0.24	−0.01	488	28.9
	$Fe_3O_4(B)$	0.65	0.01	458	60.3
	χ-Fe_5C_2	0.20	0.07	220	2.8
		0.20	0.38	186	2.2
	ε-$Fe_{2.2}C$	0.30	0.11	166	4.0
	$Fe^{2+}BO_x$	0.60	1.60		1.5
Fe-W	$Fe_3O_4(A)$	0.24	0.02	488	25.1
	$Fe_3O_4(B)$	0.64	0.02	458	51.7
	χ-Fe_5C_2	0.20	0.32	220	6.5
		0.20	−0.05	186	6.8
	ε-$Fe_{2.2}C$	0.20	0.07	165	7.1
	$Fe^{2+}BO_x$	1.33	2.24		2.8

Reaction conditions: 3.0 MPa syngas ($H_2/CO = 2$), 200 °C, 12 h.
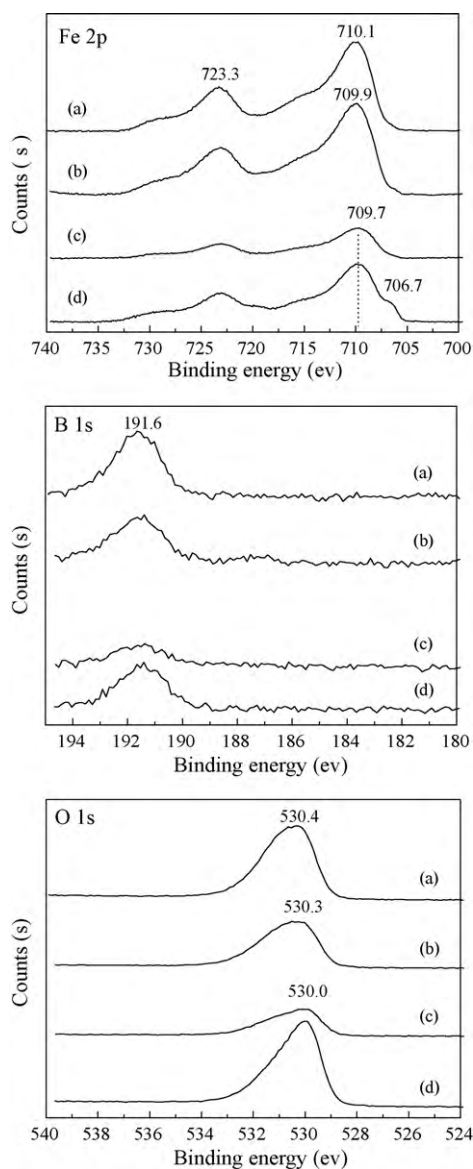
Fig. 7. XPS spectra of Fe 2p, B 1s and O 1s levels in the (a) Fe-E, (b) Fe-E2W1, (c) Fe-E1W2, and (d) Fe-W catalysts.

Table 4
FTS activity, selectivity, and hydrocarbon product distribution of the iron nanocatalysts prepared in various solvents.

Catalyst	Fe-E	Fe-E2W1	Fe-E1W2	Fe-W
Total pressure drop (MPa)	0.51	0.95	1.02	1.14
Activity				
$mol_{CO} \, mol_{Fe}^{-1} \, h^{-1}$	0.30	0.62	0.76	0.83
$mol_{H_2} \, mol_{Fe}^{-1} \, h^{-1}$	0.12	0.47	0.50	0.62
Conversion (mol%)				
CO	45.95	65.29	79.75	84.16
H_2	8.62	23.87	25.05	29.63
CO_2 selectivity (mol%)	26.65	26.61	31.75	30.07
HC distribution (wt%)				
C_1	3.55	9.09	12.00	13.37
$C_2^=$	4.98	4.09	3.47	4.49
C_2	5.51	9.83	10.81	11.27
$C_3^=$	7.48	10.18	9.59	10.07
C_3	9.88	13.53	13.47.	13.90
$C_2^=-C_4^=$	20.95	24.48	22.54	24.19
C_2-C_4	28.49	38.92	38.21	39.74
$C_5^=-C_{10}^=$	33.68	26.16	25.48	23.90
C_5-C_{10}	50.82	37.38	37.81	35.94
$C_{11}-C_{20}$	17.14	14.46	11.21	9.98
$C_{21}+$	0	0.15	0.76	0.96

Reaction conditions: 3.0 MPa syngas ($H_2/CO = 2$), 200 °C, 12 h.

form of boron was detected with a B 1s binding energy of 191.6 eV consistent with the presence of either B_2O_3 or borate. Failure to observe the elemental boron may be ascribed to its tendency to oxidize more readily than metallic iron. In addition, the O 1s peaks with a binding energy around 530 eV was asymmetric, which further indicates that different types of oxygen (iron oxide, B_2O_3 or borate) exist on the catalyst surface. According to the calculation based on XPS peak areas (listed in Table 1), the surface molar ratio of Fe to B in the catalyst sample increased with the same trend as that in the bulk phases. As a whole, the Fe content on the surface was higher than that in the bulk phase and was highest for the Fe-W catalyst.

3.4. FTS performance

FTS performance of the prepared iron nanocatalysts was measured at 200 °C and 800 rpm under syngas (initial pressure = 3.0 MPa, $H_2/CO = 2$) for 12 h. The activity, selectivity, and hydrocarbon product distribution are summarized in Table 4. The activity of these catalysts increased in the following order:

Fe-E < Fe-E2W1 < Fe-E1W2 < Fe-W. Similarly, the CO conversion increased directly from 46 to 84% with increasing water added to the preparation solvent. Of the four catalysts, the catalyst prepared in water exhibited the highest FTS activity (0.83 $mol_{CO} \, mol_{Fe}^{-1} \, h^{-1}$ or $0.41 \times 10^{-5} \, mol_{CO} \, g_{Fe}^{-1} \, s^{-1}$) which was about two times that of Co nanoparticles in ionic liquids ($0.2 \times 10^{-5} \, mol_{CO} \, g_{Co}^{-1} \, s^{-1}$, 210 °C, 20 h) [17].

The Fe-E catalyst with the smallest particles showed the lowest activity, which can be attributed to the coagulation of nanoparticles during FTS. Herein, the correlation of the catalytic activities to the particle sizes of the four catalysts suggests that the particle size is not the only factor affecting activity. The stabilizing effect of the solvent may play a key role during FTS reaction and the structural properties of these catalysts must be also taken into consideration. The variation of 3d electron densities from B to Fe in Fe-B alloys made relatively electron-rich iron sites. Richness in electron were favorable for activating the adsorbed CO molecules through an electron back-donation from d orbitals of Fe to the π^* antibonding orbital of CO. It has been demonstrated that the catalyst activity during FTS is correlated with the formation of active phases. The iron-based catalysts experience a series of complicated micro-structural changes during reduction and FTS reaction. In generally, it is recognized that metallic iron, iron carbides and iron oxides coexist after activation and during FTS reaction. Iron carbide species are the most likely active phases for an iron-based catalyst [30]. Thus the content of iron carbides can be used to monitor the formation of FTS active sites to some extent. Based on Mössbauer spectra results, the catalyst prepared with more water in the preparation system is expected to exhibit higher FTS activity. This agrees with the activity data discussed in this section. Since the structural transformation of the catalysts occurred primarily on the surface, the surface property is also of vital importance to catalytic performance. Surfaces with higher iron content will potentially expose more active sites. The higher the extent of iron reduction on the surface, the more easily the catalyst surface will carbonize during FTS reaction. For the Fe-W catalyst, the high FTS activity can be attributed to both high iron content and high extent of reduction on the surface resulting in the formation of the most iron carbides.

Hydrocarbon product distribution from the catalysts (listed in Table 4) suggest that C_2-C_{10} light hydrocarbons made up the majority (more than 70 wt%) of the products. The four catalysts
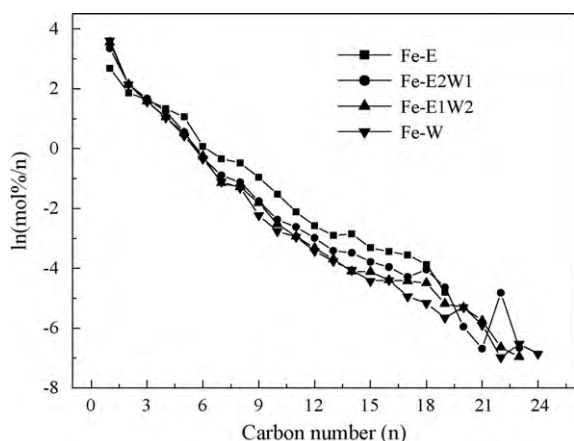
Fig. 8. Quasi-ASF distributions of hydrocarbon products for the catalysts prepared in various solvents.

showed higher selectivity to light olefins ($C_2^=$–$C_4^=$ and $C_5^=$–$C_{10}^=$) and lower selectivity to $C_{21}+$ products indicating that the catalysts strongly inhibited hydrogenation. Under typical conditions for our experiments, FTS reactions favored chain termination and the production of light hydrocarbons. In addition, methane and C_2–C_4 selectivity increased slightly while C_{11}–C_{20} selectivity decreased gradually with increasing water added to the preparation system. Quasi-Anderson–Schulz–Flory (ASF) plots were drawn for the four catalysts (shown in Fig. 8). The trends of these plots were similar to those of ASF but with improved linearity [31]. In other words, the chain length distribution of the products followed ASF statistics. According to the ideal ASF equation, ideal molecular weight distribution should give a straight line. In practice, the majority of the reported ASF plots showed a nearly straight line only in the C_4–C_{12} region. Marked deviations from ideal ASF distribution are observed in the C_1–C_3 range. The methane is usually more than predicted, particularly over Co and Ru catalysts. Over Ru and Co catalysts, the C_2 and C_3 products are much less than predicted while over Fe only slightly less [32]. In our experiment, there were little deviations from ideal ASF distribution in the C_1–C_3 range. These data for C_1–C_3 are slightly different from classic FTS data. The following aspects should be considered. First, the activity of olefins secondary reaction especially for ethene is relatively low at lower reaction temperature. As a result, little deviations from ideal ASF distribution were observed for C_2 products [33]. In addition, the solvent, iron nanosized catalysts and the batch mode may have a significant effect on the product selectivity [32,34]. These factors may explain why the chain length distribution of the products followed basically ASF statistics in the present work.

After reaction, cyclohexane was added to extract the products. The upper phase containing hydrocarbon products were easily separated from the PEG/catalyst system in the bottom of the reactor by simple decantation. ICP-AES was used to check catalyst leaching during extraction. No detectable iron in the hydrocarbon layer was found indicating a negligible loss of catalysts during the extraction procedure. The nanoparticles were finally separated from the residual reaction solution using a permanent magnet. In a word, using PEG as the solvent for FTS significantly simplified product/catalyst separation.

4. Conclusion

Iron nanocatalysts were prepared by KBH_4 reduction of Fe^{3+} in various solvents, viz., ethylene glycol, ethylene glycol/water and water. FTS reaction was carried out over these catalysts using PEG (400) as the reaction medium under mild conditions (3.0 MPa syngas, $H_2/CO = 2$, 200 °C). The as-prepared nanocatalysts were mainly composed of amorphous Fe-B or Fe-B/α-Fe, and the α-Fe content increased with the addition of water in the solvent. Results of FTS activity indicated that the catalyst prepared in water displayed high CO conversion due to its high iron concentration and extent of reduction on the surface. MES showed a much higher iron carbide composition in the catalyst prepared in water after FTS reaction suggesting that iron carbides may play an important role in this nano-catalyzed liquid system.

References

[1] A.A. Adesina, Appl. Catal. A 138 (1996) 345.
[2] H. Schulz, Appl. Catal. A 186 (1999) 3.
[3] Z. Hu, Y. Fan, Y. Chen, Appl. Phys. A-Mater. Sci. Proc. 68 (1999) 225.
[4] Y.W. Chen, N. Sasirekha, Y.C. Liu, J. Non-Cryst. Solids 355 (2009) 1193.
[5] H. Li, J. Liu, S.H. Xie, M.H. Qiao, W.L. Dai, H.X. Li, J. Catal. 259 (2008) 104.
[6] A.M. Saib, A. Borgna, J. van de Loosdrecht, P.J. van Berge, J.W. Geus, J.W. Niemantsverdriet, J. Catal. 239 (2006) 326.
[7] H. Choi, S.R. Al-Abed, S. Agarwal, D.D. Dionysiou, Chem. Mater. 20 (2008) 3649.
[8] W. Chen, Z. Fan, X. Pan, X. Bao, J. Am. Chem. Soc. 130 (2008) 9414.
[9] L.S. Ott, R.G. Finke, Coord. Chem. Rev. 251 (2007) 1075.
[10] J.H. Lee, K.E. Cha, M.S. Kim, H.W. Hong, D.J. Chung, G. Ryu, H. Myung, Toxicol. Lett. 190 (2009) 202.
[11] B.P.S. Chauhan, J.S. Rathore, T. Bandoo, J. Am. Chem. Soc. 126 (2004) 8493.
[12] M. Salavati-Niasari, Z. Fereshteh, F. Davar, Polyhedron 28 (2009) 126.
[13] J.A. Widegren, R.G. Finke, Inorg. Chem. 41 (2002) 1558.
[14] C.X. Xiao, H.Z. Wang, X.D. Mu, Y. Kou, J. Catal. 250 (2007) 25.
[15] J. Schulz, A. Roucoux, H. Patin, Chem. Commun. (1999) 535.
[16] C.X. Xiao, Z.P. Cai, T. Wang, Y. Kou, N. Yan, Angew. Chem. Int. Ed. 47 (2008) 746.
[17] D.O. Silva, J.D. Scholten, M.A. Gelesky, S.R. Teixeira, A.C.B. Dos Santos, E.F. Souza-Aguiar, J. Dupont, Chemsuschem. 1 (2008) 291.
[18] W. Wang, Z.H. Jin, T.L. Li, H. Zhang, S. Gao, Chemosphere 65 (2006) 1396.
[19] S. Chandrasekhar, C. Narsihmulu, S.S. Sultana, N.R. Reddy, Org. Lett. 4 (2002) 4399.
[20] S. Chandrasekhar, S.J. Prakash, C.L. Rao, J. Org. Chem. 71 (2006) 2196.
[21] B. Rajesh, N. Sasirekha, Y.W. Chen, S.P. Lee, Ind. Eng. Chem. Res. 46 (2007) 2034.
[22] G.N. Glavee, K.J. Klabunde, C.M. Sorensen, G.C. Hadjipanayi, Inorg. Chem. 34 (1995) 28.
[23] G. Barault, J.M. Greneche, Solid State Commun. 96 (1995) 155.
[24] V.A. Barinov, V.A. Tsurin, V.I. Voronin, S.I. Novikov, V.T. Surikov, Phys. Met. Metallogr. 101 (2006) 456.
[25] J. Balogh, L. Bujdoso, T. Kemeny, I. Vincze, J. Phys.: Condens. Matter 9 (1997) L503.
[26] A. Martino, M. Stoker, M. Hicks, C.H. Bartholomew, A.G. Sault, J.S. Kawola, Appl. Catal. A 161 (1997) 235.
[27] Z.H. Suo, Y. Kou, J.Z. Niu, W.Z. Zhang, H.L. Wang, Appl. Catal. A 148 (1997) 301.
[28] C.H. Zhang, Y. Yang, Z.C. Tao, T.Z. Li, H.J. Wan, H.W. Xiang, Y.W. Li, Acta Phys.-Chim. Sin. 22 (2006) 1310.
[29] X. An, B.S. Wu, W.J. Hou, H.J. Wan, Z.C. Tao, T.Z. Li, Z.X. Zhang, H.W. Xiang, Y.W. Li, B.F. Xu, F. Yi, J. Mol. Catal. A 263 (2007) 266.
[30] E.d. Smit, B.M. Weckhuysen, Chem. Soc. Rev. 37 (2008) 2758.
[31] A. Tavakoli, M. Sohrabi, A. Kargari, Chem. Eng. J. 136 (2008) 358.
[32] I. Puskas, R.S. Hurlbut, Catal. Today 84 (2003) 99.
[33] G.P. van der Laan, A.A.C.M. Beenackers, Catal. Rev. 41 (1999) 255.
[34] X.H. Liu, W.S. Linghu, X.H. Li, K.J. Asami, K.R. Fujimoto, Appl. Catal. A 303 (2006) 251.